Supplementary Information:

Kennett & Liang (2021). Australian Journal of Earth Sciences, 68(5)
https://doi.org/10.1080/08120099.2021.1837955

The transition from the Thomson Orogen to the North Australian Craton from seismic data.

Brian L.N. Kennett[a] and Shasha Liang[b]

[a] Research School of Earth Sciences, The Australian National University, Canberra ACT 2601, Australia
[b] Inner Mongolia Seismological Bureau & Inner Mongolia University of Technology, China

S1. Extracting P reflectivity from teleseismic records

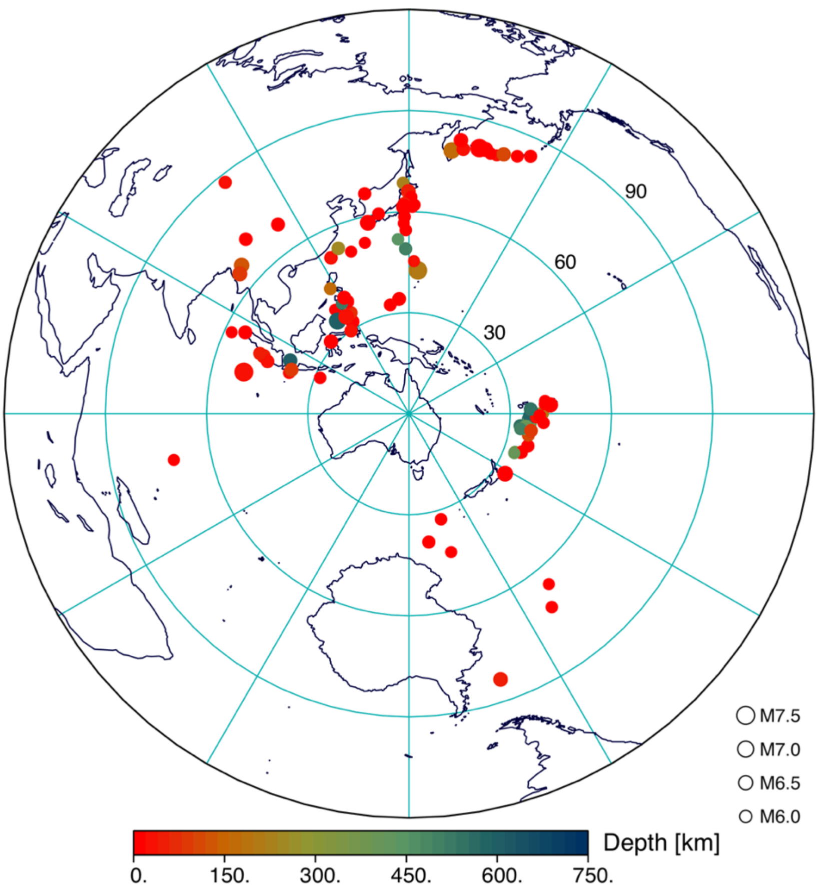

Figure S1: Distribution of the 100 teleseismic earthquakes used relative to the AQT deployment

The AQT deployment of 79 stations recorded 100 teleseismic events with magnitude greater than 6 during 2016–2017, whose distribution is shown in Figure S1, though not all stations record each event. The absence of events in the SW quadrant means that the crustal sampling around the stations is biased towards the north and the east since many events occurred in the Tonga-Fiji subduction zone.

The P wave reflectivity results are obtained by constructing the autocorrelation of the portion of the recorded seismograms containing the teleseismic P wave arrival and the 100 s of following coda. This requires the selection of arrivals with good signal to noise, assessed by comparison of the P signal and the preceding noise. The instrumental response is removed from each trace and autocorrelation is performed on a 120 s time window. A bandpass filter is then applied to select higher frequency components and suppress the zero-lag peak in the autocorrelation. The ray path associated with each arriving P wave is calculated for a reference model and the time-domain autocorrelation is projected into depth along this path. The ray paths for all events at a station (or a group of stations) are then projected onto a defined profile, and the autocorrelation amplitudes are stacked in bins of specified width determined by the frequency band and the spacing of stations.

S2. Additional Profiles

In the main paper we have illustrated a group of NS profiles from the eastern part of the AQT deployment (G4, G5, G7, G8). Figure S2 presents equivalent results from the western group (G1, G2, G3).

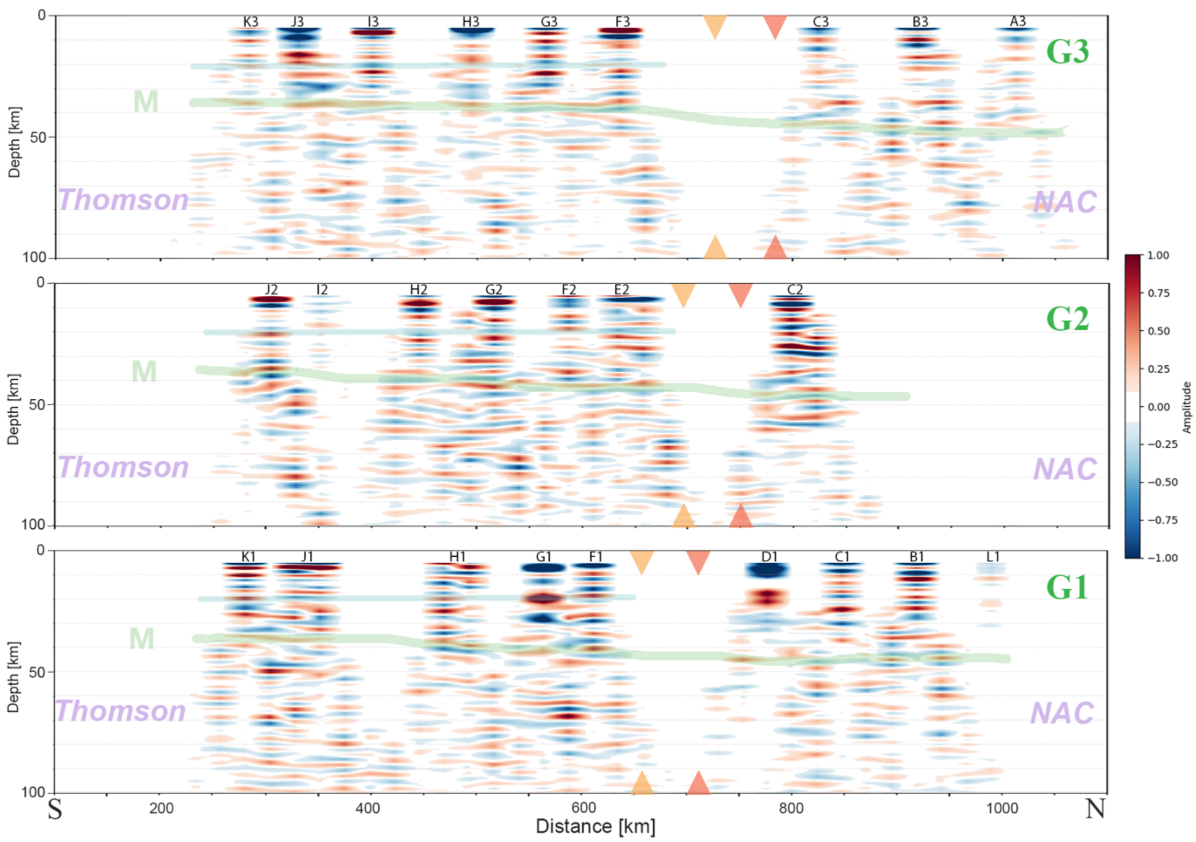

Figure S2: Reflection imaging from teleseismic arrivals for the frequency band from 0.1–2.0 Hz, projected on to the profiles G1, G2, and G3 indicated in Figures 1 and S3. Depth conversion in migration uses the *ak135* model (Kennett et al., 1995). The light green bands indicate the variation of the Moho along the profiles. A light blue marker is placed for reference at 20 km depth in the Thomson Orogen. The red and orange markers indicate the likely extent of the transition zone between the Thomson Orogen and the North Australian Craton.

Once again there is a significant change in reflection character between the stations in the Thomson Orogen and those in the North Australian Craton. On profile G1, in particular, the Crust tends to thicken before the transition to the North Australian Craton is reached.

The configuration of the AQT stations is displayed in Figure S3 to allow identification of stations on the profiles in Figures 5, 6 and S2.

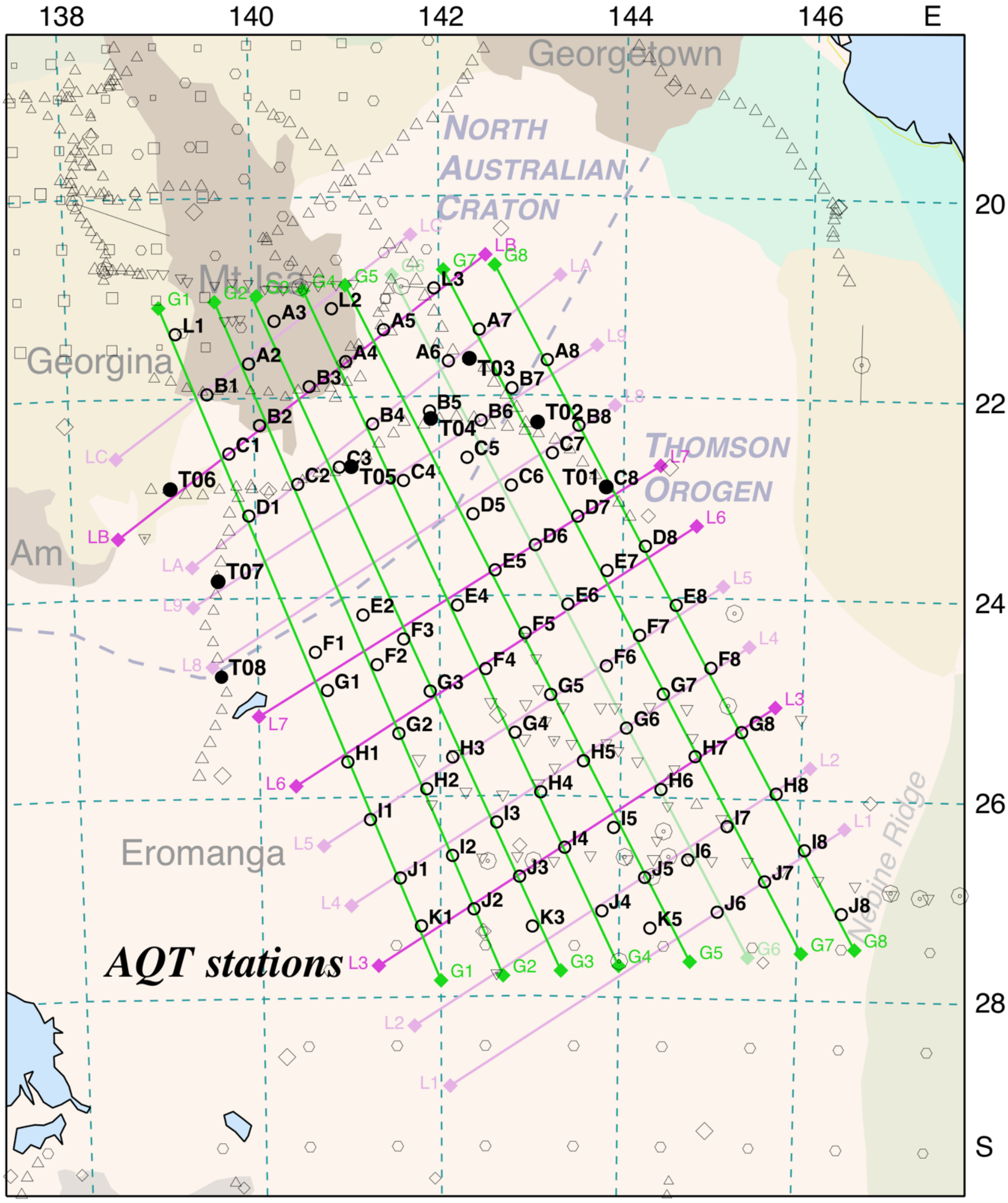

Figure S3: Station configuration for AQT experiment. The stations shown with solid symbols placed on the CF reflection profiles were fully broad-band installations. The profiles illustrated in Figures 5,6 and S2 are shown with stronger coloured lines.

The Moho estimates extracted from the autocorrelation stacks for the AQT stations are presented in Table S1 together with the weighting applied in Moho surface construction. Each estimate is based on independent assessments from projections onto the NS and EW profiles, equivalent to low-fold reflection stacks, and based on the transition from crustal reflectivity to that of the upper mantle. Because the estimates are made from isolated stations, assigned weights are relatively low. As noted above, the sampling from the distant events means that the values will represent structure slightly to the north and east of the station location.

Table S1: Moho depth estimates [km] and weighting for AQT stations

Station	**Latitude**	**Longitude**	**Moho**	**Weight**	**Station**	**Latitude**	**Longitude**	**Moho**	**Weight**
AQTA3*	-21.2518	140.2364	43.0	0.65	AQTG7	-24.9816	144.4620	39.4	0.60
AQTA4*	-21.6638	140.9992	40.7	0.55	AQTG8	-25.3524	145.3331	40.6	0.65
AQTA5*	-21.3479	141.4088	44.7	0.60	AQTH1	-25.6633	140.9753	38.6	0.65
AQTA7*	-21.3458	142.4341	39.2	0.65	AQTH2	-25.9378	141.8491	36.6	0.65
AQTA8†	-21.6495	143.1655	40.7	0.65	AQTH3	-25.6207	142.1378	38.6	0.65
AQTB1*	-21.9738	139.5003	42.8	0.60	AQTH4	-25.9677	143.1147	38.3	0.63
AQTB3*	-21.9100	140.6035	42.2	0.60	AQTH5	-25.6555	143.5871	36.7	0.65
AQTB4*	-22.2877	141.2824	42.3	0.60	AQTH6	-25.9350	144.4499	41.4	0.63
AQTB5*	-22.1627	141.8971	39.7	0.65	AQTH7	-25.6015	144.8235	38.3	0.65
AQTB7*	-21.9314	142.7857	40.0	0.65	AQTH8	-25.9603	145.7303	42.3	0.55
AQTB8†	-22.3032	143.5103	41.6	0.60	AQTI2	-26.6040	142.1333	35.6	0.57
AQTC1*	-22.5687	139.7240	43.6	0.60	AQTI3	-26.2700	142.6262	36.6	0.65
AQTC2*	-22.8827	140.4648	46.3	0.60	AQTI4	-26.5202	143.3849	37.3	0.65
AQTC3*	-22.7171	140.9175	43.0	0.60	AQTI5	-26.3190	143.9285	39.4	0.60
AQTC4*	-22.8553	141.6118	42.6	0.55	AQTI6	-26.6335	144.7603	39.6	0.55
AQTC5*	-22.6266	142.3024	39.0	0.65	AQTI7	-26.2943	145.1919	37.7	0.65
AQTC7†	-22.5796	143.2252	39.1	0.65	AQTI8	-26.5186	146.0603	42.2	0.60
AQTD1*	-23.1921	139.9280	42.4	0.65	AQTJ1	-26.8264	141.5488	36.8	0.65
AQTD5†	-23.1907	142.3650	37.4	0.65	AQTJ2	-27.1375	142.3724	36.1	0.60
AQTD7†	-23.2112	143.5041	37.5	0.65	AQTJ3	-26.8112	142.8826	37.4	0.65
AQTD8	-23.5056	144.2437	38.3	0.65	AQTJ4	-27.1525	143.8063	36.0	0.60
AQTE2†	-24.1974	141.1590	40.0	0.60	AQTJ5	-26.8145	144.2810	40.6	0.65
AQTE4†	-24.1028	142.1947	38.7	0.55	AQTJ6	-27.1505	145.0990	40.4	0.57
AQTE5†	-23.7512	142.6063	36.4	0.60	AQTJ7	-26.8384	145.6230	39.8	0.65
AQTE6	-24.0907	143.4033	38.9	0.65	AQTJ8	-27.1461	146.4915	41.3	0.65
AQTE7	-23.7520	143.8283	36.8	0.65	AQTK1	-27.3059	141.7822	36.3	0.65
AQTE8	-24.0921	144.5890	37.7	0.65	AQTK3	-27.3081	143.0280	37.0	0.63
AQTF1†	-24.5646	140.6326	43.0	0.60	AQTK5	-27.3199	144.3472	37.7	0.63
AQTF2†	-24.6948	141.3096	41.3	0.63	AQTL1*	-21.3657	139.1746	44.9	0.55
AQTF3†	-24.4400	141.6029	37.1	0.65	AQTL2*	-21.1336	140.8525	47.8	0.60
AQTF4	-24.7379	142.5040	39.0	0.60	AQTL3*	-20.9339	141.9497	42.6	0.55
AQTF6	-24.7048	143.8317	37.0	0.60	AQT01†	-22.9174	143.8113	41.8	0.65
AQTF8	-24.7158	144.9813	37.8	0.65	AQT02†	-22.2725	143.0632	41.3	0.55
AQTG1†	-24.9475	140.7598	40.7	0.65	AQT03*	-21.6381	142.3282	40.6	0.60
AQTG2	-25.3829	141.5433	41.3	0.65	AQT04*	-22.2372	141.9106	41.6	0.60
AQTG3	-24.9619	141.8919	38.8	0.60	AQT06*	-22.9126	139.0811	40.0	0.60
AQTG4	-25.3734	142.8288	39.4	0.63	AQT07*	-23.8422	139.5796	43.6	0.65
AQTG5	-24.9952	143.2199	36.7	0.60	AQT08†	-24.7972	139.5949	41.4	0.65

* Stations on the North Australian Craton   † Stations in transitional region

Unmarked stations lie in the Thomson orogen.

S3. Moho surface

The Moho surface displayed in Figure 6 has been constructed using the procedure developed by Kennett (2019) in which the estimate of the local Moho at a spatial point is constructed from a sum of contributions from all available data points with allowance for weighting and the distance of these data points from the sample point. For different data sets we assign internal weights based on the quality of the result, e.g., for reflection picks we have used A = 0.9, B = 0.8, C = 0.7, D = 0.6. All points in the same data set are then assigned a Gaussian spread function with decay rate defined by a spatial spread value specific to the class of data. The information from different data sets is combined allowing for relative weighting between data sets as in Table S2.

Table S2: Weighting used in construction of Moho surface

Data Type	*Dataset weighting*	*Angular spread (°)*
Prior model	0.05	0.4
Refraction	0.7	1.0
Receiver Functions	0.9-1.0	0.4
Reflection	1.0	0.25
Autocorrelations – continuous data	1.0	0.6
Autocorrelations – teleseismic stacks	1.0	0.6

We have found it convenient to use prior models with very low weights so that we avoid 'holes' in the Moho surface. For the present study we have used the Moho surface derived by Aitken et al. (2013) from gravity inversion that provides full continental coverage, and also a good definition of the continent-ocean transition. The downweighting of the refraction results occurs because we have endeavoured to provide two spatial separated values for each refraction experiment to allow for the directional sampling inherent in the technique.

In addition to the data value at a point, we can make an estimate of the consistency of the various data sets by constructing a variance estimate at each sample location, using the weighted value for the square of the samples, and the square of the sample estimate. The weighted estimate is constructed using the same combination of dataset and spatial weighting.

As a measure of the likely error in a spatial value, the uncertainty values for the various data points can be combined in the same way as the data values. For the Moho estimates we do not have a direct uncertainty measure for all points, but in every case have a quality proxy. We have followed Kennett (2019) to use an empirical relation, calibrated against receiver function results, to give an uncertainty e in kilometres from a data weight w:
$e = 0.8 + 6.0 * (1 - w)$.

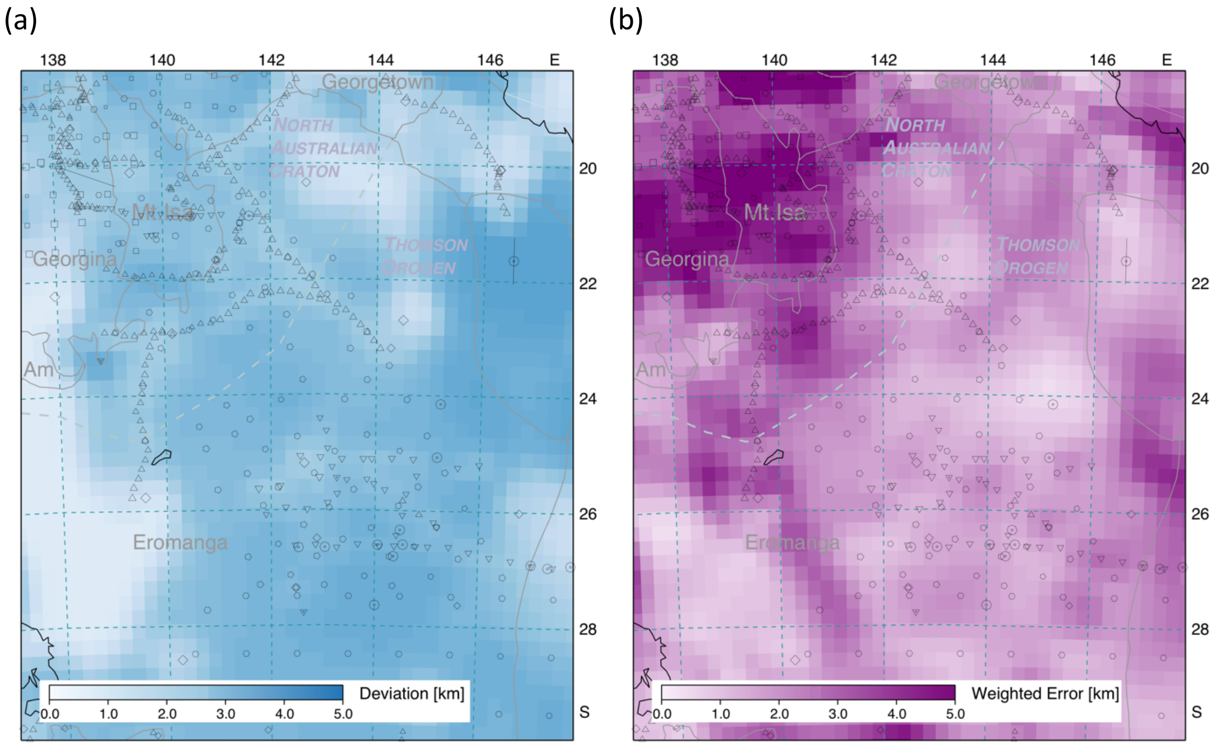

Figure S4: Measures of the consistency and uncertainty in the estimated Moho surface across the region. (a) The consistency of Moho values using the standard deviation of the deviations. (b) Weighted uncertainty distribution.

In Figure S4 we show the consistency and uncertainty estimates associated with Moho surface displayed in Figure 7. We have superimposed the distribution of the data points in the region using the same symbols as in Figure 5. The strong spatial correlation of the reflection data is apparent, but can be disrupted by close discordant Moho depth estimates from other techniques that have a broader spatial sampling. The weighted error tends to be largest on the fringe of sampled areas, but is significant in the Mt. Isa region where the crust is thick, with an often-indistinct base, and a wide variety of different approaches have been used to estimate crust thickness.

References:

Aitken, A.R.A., Salmon, M.L., & Kennett, B.L.N. (2013). Australia's Moho: A test of the usefulness of gravity modelling for the determination of Moho depth, *Tectonophysics*, *609*, 468–479; doi: 10.1016/j.tecto.2012.06.049

Kennett, B.L.N. (2019). Areal parameter estimates from multiple datasets. *Proceedings of the Royal Society A*, *475*, 20190352; doi: 10.1098/rspa.2019.0352

Kennett, B.L.N., Engdahl, E.R., Buland, R. (1995). Constraints on seismic velocities in the Earth from travel times, *Geophys. J. Int., 122*, 108–124.